research papers

Recent advances in the development of high-resolution 3D cadmium–zinc–telluride drift strip detectors

Leonardo Abbene,[a]* Gaetano Gerardi,[a] Fabio Principato,[a] Antonino Buttacavoli,[a] Saverio Altieri,[b,c] Nicoletta Protti,[b,c] Elio Tomarchio,[d] Stefano Del Sordo,[e] Natalia Auricchio,[f] Manuele Bettelli,[g] Nicola Sarzi Amadè,[g] Silvia Zanettini,[h] Andrea Zappettini[g] and Ezio Caroli[f]

[a]Department of Physics and Chemistry (DiFC), University of Palermo, Viale delle Scienze, Edificio 18, Palermo 90128, Italy, [b]Nuclear Physics National Institute (INFN), Unit of Pavia, via Agostino Bassi 6, Pavia 27100, Italy, [c]Department of Physics, University of Pavia, via Agostino Bassi 6, Pavia 27100, Italy, [d]Department of Engineering, University of Palermo, Viale delle Scienze, Edificio 6, Palermo 90128, Italy, [e]INAF/IASF Palermo, Palermo Italy, [f]INAF/OAS Bologna, Bologna, Italy, [g]IMEM/CNR, Parco Area delle Scienze 37/A, Parma 43100, Italy, and [h]due2lab s.r.l., Via Paolo Borsellino 2, Scandiano, Reggio Emilia 42019, Italy. *Correspondence e-mail: leonardo.abbene@unipa.it

In the last two decades, great efforts have been made in the development of 3D cadmium–zinc–telluride (CZT) detectors operating at room temperature for gamma-ray spectroscopic imaging. This work presents the spectroscopic performance of new high-resolution CZT drift strip detectors, recently developed at IMEM-CNR of Parma (Italy) in collaboration with due2lab (Italy). The detectors (19.4 mm × 19.4 mm × 6 mm) are organized into collecting anode strips (pitch of 1.6 mm) and drift strips (pitch of 0.4 mm) which are negatively biased to optimize electron charge collection. The cathode is divided into strips orthogonal to the anode strips with a pitch of 2 mm. Dedicated pulse processing analysis was performed on a wide range of collected and induced charge pulse shapes using custom 32-channel digital readout electronics. Excellent room-temperature energy resolution (1.3% FWHM at 662 keV) was achieved using the detectors without any spectral corrections. Further improvements (0.8% FWHM at 662 keV) were also obtained through a novel correction technique based on the analysis of collected-induced charge pulses from anode and drift strips. These activities are in the framework of two Italian research projects on the development of spectroscopic gamma-ray imagers (10–1000 keV) for astrophysical and medical applications.

1. Introduction

The desire for room-temperature gamma-ray spectroscopic imagers with sub-millimetre spatial resolution in 3D and energy resolutions close to the superb resolutions of cooled high-purity germanium (HPGe) detectors (0.3% FWHM at 662 keV) (Abbene et al., 2013a,b; Knoll, 2000) has stimulated intense research activities on the development of 3D cadmium–zinc–telluride (CdZnTe or CZT) detectors. Room-temperature measurements of photon energy, timing and 3D positioning up to the megaelectronvolt region are key requirements for several applications in astrophysics (Kuvvetli et al., 2010), medical imaging (Abbaszadeh et al., 2016; Drezet et al., 2007; Peng & Levin, 2010) and nuclear security (Johns & Nino, 2019; Wahl & He, 2011, 2015). Since the first spectroscopic grade detector was fabricated (Butler et al., 1992), CZT now represents the leading detector material over high-Z and wide-band-gap compound semiconductors (Del Sordo, 2004, 2009; Johns & Nino, 2019; Owens & Peacock, 2004; Principato
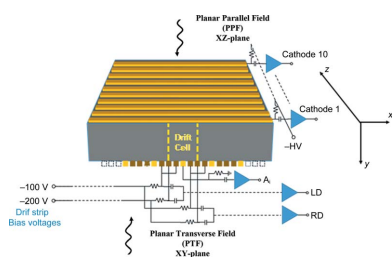
et al., 2013; Takahashi & Watanabe, 2001; Turturici *et al.*, 2014). Aside from its appealing physical properties (high atomic number, wide band gap, high density), this success can mainly be attributed to the important advancements in both crystal growth and device fabrication technologies (Abbene *et al.*, 2016, 2020; Chen *et al.*, 2008; Iniewski, 2014; Prokesch *et al.*, 2018; Szeles *et al.*, 2008; Thomas *et al.*, 2017; Veale *et al.*, 2020; Zappettini *et al.*, 2009).

In general, 3D CZT detectors are developed through different approaches. Sub-millimetre spatial resolution and excellent energy resolution (<1% FWHM at 661.7 keV, after spectral correction) are obtained with pixelated (He *et al.*, 1999; Kim *et al.*, 2011; Zhang *et al.*, 2012) and virtual Frisch-grid (Bolotnikov *et al.*, 2020) CZT detectors. In this case, the detectors are used in parallel planar field (PPF) geometry, *i.e.* irradiated through the cathode, producing 3D positioning through the pixels/pads and the cathode-to-anode (C/A) ratio. Interesting results are also obtained using CZT drift strip detectors (Budtz-Jørgensen & Kuvvetli, 2017; Caroli *et al.*, 2010; Howalt Owe *et al.*, 2019; Kalemci & Matteson, 2002; Kuvvetli *et al.*, 2010). Here the detectors are used in planar transverse field (PTF) geometry and give 2D positioning through cross-strip electrode patterns on the cathode/anode electrodes and the third coordinate through the C/A ratio. This last approach is more conservative than pixelated detectors regarding the number of readout channels.

Developing readout electronics for 3D CZT detectors is generally a difficult task due to the complex processing required to analyse the wide variety of different pulse shapes produced by these detectors. A wide variety of different induced/collected charge pulses is typically generated by 3D CZT detectors, related to the particular electrode patterns and to the different mechanisms in pulse formation (drift, induction, charge trapping, charge sharing and cross talk). Currently, the digital pulse processing (DPP) approach, which works on digitized detector pulses, allows dedicated pulse analysis and better results than conventional analog electronics (Bolotnikov *et al.*, 2014; Howalt Owe *et al.*, 2019; Zhu *et al.*, 2011).

Recently, in the framework of two Italian research projects (3DCaTM and 3CaTS projects, funded by ASI and INFN, respectively), new high-resolution 3D CZT drift strip detectors have been developed. The goal of the 3CaTS project (Fatemi *et al.*, 2018) is to develop a new single-photon emission computed tomography (SPECT) system for real-time therapeutic dose monitoring in the binary hadron therapy termed boron neutron capture therapy (BNCT). The 3DCaTM project (Caroli *et al.*, 2019) foresees the realization of detectors able to provide simultaneous spectroscopy (10–1000 keV), imaging, timing and scattering polarimetry as both focal plane detectors on a space telescope implementing new high-energy optics (*e.g.* broadband Laue lens), and small wide-field instruments to be used on clusters of micro-satellites. The 3D CZT drift strip detectors (19.4 mm × 19.4 mm × 6 mm), fabricated with a new surface passivation technique, are characterized by very low-leakage currents between the drift strips, allowing the application of high-drift bias voltages with

strong benefits in charge collection efficiency and energy resolution.

In this work, we will present, for the first time, the spectroscopic abilities of these new detectors coupled to custom 32-channel digital readout electronics. All output pulses from the anode, cathode and drift strips, measured in temporal coincidence, were processed with dedicated analysis. The key features of the induced/collected charge pulses will be investigated by means of simulations and measurements, focusing on their role of detector performance enhancements. We will show two main results. First, the detectors are characterized by excellent room-temperature energy resolution without spectral corrections due to the successful fabrication technique; second, further spectroscopic improvements will be presented by means of a new digital spectral correction technique.

2. The drift strip detectors

The concept of drift or steering electrodes was pioneered by Gatti and Rehak in 1983 for silicon radiation detectors (Gatti & Rehak, 1984*a*,*b*). This approach, combined with the electron charge sensing electrode geometries of the detectors (pixels, strips, circular rings), was successfully used in CZT detectors with strong improvements in charge collection efficiency and energy resolution (Abbene *et al.*, 2007; Alruhaili *et al.*, 2014; Lingren *et al.*, 1998; Owens *et al.*, 2007; Kalemci & Matteson, 2002; Kuvvetli & Budtz-Jorgensen, 2005; Van Pamelen *et al.*, 1998). Recently, new CZT drift strip detectors were realized at IMEM-CNR of Parma (Parma, Italy; http://www.imem.cnr.it) in collaboration with due2lab (Reggio Emilia, Italy; http://www.due2lab.com). The detectors were fabricated from CZT crystals (19.4 mm × 19.4 mm × 6 mm) grown by the travelling heather method (THM) technique. More specifically, the prototypes were realized starting from Redlen CZT pixel detectors after electrode removal and surface treatments. As is well known (Chen *et al.*, 2008; Iniewski, 2014), Redlen (http://redlen.ca) is able to produce spectroscopic grade CZT crystals with excellent charge-transport properties (mobility-lifetime products of electrons $\mu_e \tau_e > 10^{-2}$ cm^2 V^{-1}). In this work, we used CZT materials characterized by $\mu_e \tau_e$ ranging from 1×10^{-2} cm^2 V^{-1} to 3×10^{-2} cm^2 V^{-1}. The anode layout is characterized by gold-strip electrodes with a pitch of 0.4 mm (0.15 mm strip width and 0.25 mm inter-strip gap) (top of Fig. 1); however, the cathode side is divided into ten gold strips orthogonal to the anode strips with a pitch of 2 mm (1.9 mm strip width and 0.1 mm inter-strip gap), as shown in Fig. 1 (bottom). The anode strips are organized into collecting strips (1.6 mm pitch) and groups of three drift strips between each collecting strip. The drift strips are negatively biased to optimize electron charge collection at the collecting strips. The key goal in CZT drift strip detector development is to allow the application of high bias voltages between the drift strips in order to optimize electron charge collection, maintaining the leakage currents (*i.e.* the electronic noise) to be as low as possible. To obtain this, great efforts were made by our group in developing new detector processing techniques. The realization of a drift strip
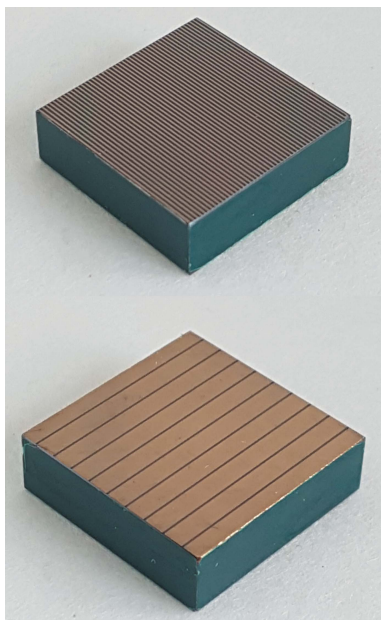
Figure 1
Anode (top) and the cathode (bottom) layouts of the CZT drift strip detectors. The anode strips (0.4 mm pitch; 0.25 mm gap) are orthogonal to the cathode strips (2 mm pitch; 0.1 mm gap). The anode strips are organized into collecting strips (1.6 mm pitch) and drift strips (0.4 mm pitch) which are negatively biased to optimize electron charge collection.

structure is generally a challenging procedure; first, it requires a double-patterning processing in segmenting both the cathode and the anode; second, the surface passivation is a critical operation in order to reduce the leakage currents. Regarding our detectors, the CZT crystals were lapped with abrasive SiC paper, polished and extensively cleaned before starting the cleanroom process. The cathode strips are patterned by means of wet-chemical electroless gold deposition, standard photolithography and subsequent Br-based etching in ethylene glycol of the gap between the strips. On the anode side, a dedicated surface passivation procedure was applied in two steps: (i) deposition of negative photoresist with the anode pattern on the as-polished CZT surface and (ii) strip deposition by means of the wet-chemical electroless technique from methanol solution, after a short Br-based etching for surface oxide removal. This lithographic process for the anode side is challenging if one considers that Au electroless deposition is carried out in alcoholic solution (instead of typical water solution) after photolithographic patterning. Indeed, Au electroless deposition from methanol provides better mechanical adhesion than water-based deposition (Benassi *et al.*, 2017), and patterning of the electrodes prior to Au deposition avoids a detrimental etching step and ensures lower leakage currents than the common wet passivation techniques. In our case, the detectors are characterized by very low-leakage currents between the drift strips (<1 nA at 50 V and twice this value at 100 V) and uniformity among them. Fig. 2 highlights the final packaging of the detectors. The sensor unit support and electrical interface board consist of five superimposed layers of different materials (Roger, Kapton and FR4) and are rolled together. By
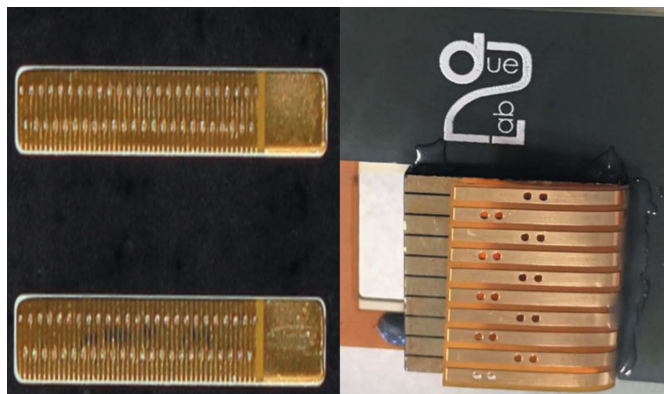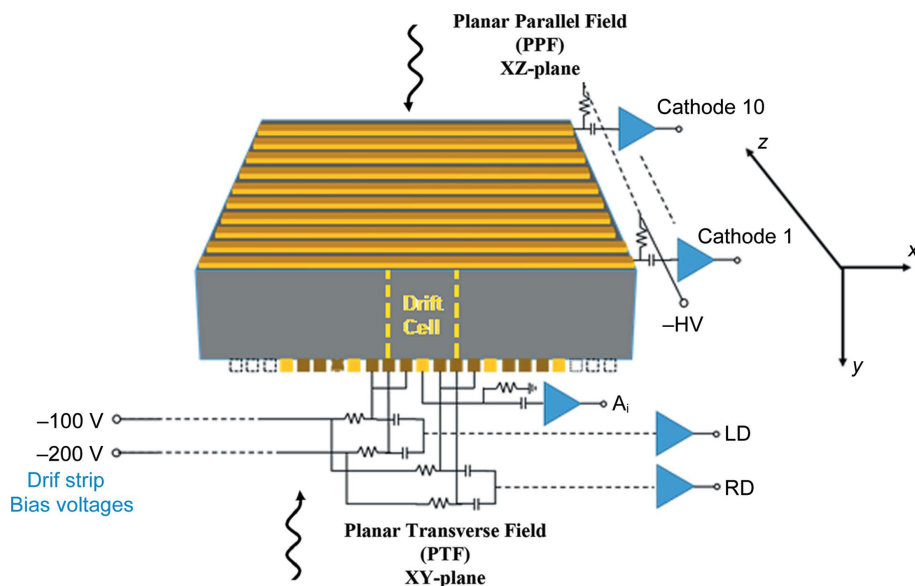

Figure 2
Overview of the anode (left) and cathode (right) electrode bonding of the 3D drift strip CZT detectors.

means of a non-trivial bonding procedure, each metallic strip of the 3D CZT sensor is electrically connected with conductive glue to Au lines insulated by Kapton film.

With regards to the working mode, each detector is characterized by 12 drift cells; as shown in Fig. 3, each drift cell is defined by 15 strips: a collecting anode strip surrounded by two drift strips on the right side (RD), two on the left side (LD) and ten cathode strips. The two most external drift strips are actually shared between adjacent drift cells. The central drift strip of each group of three is more negatively biased than the two drift strips close to the collecting anodes. The dimensions of a single drift cell are 1.6 mm × 6 mm × 20 mm. The anode drift strips and the cathode strips are negatively biased to focus the electrons toward the collecting anode. Regarding the signal readout, the drift strips are connected in two groups of LD and RD drift strips. Each group contains three drift strips. Therefore, a drift cell is characterized by 13 readout channels. Overall, each detector drives 24 readout channels (12 collecting anode strips, 10 cathode strips and 2 drift anode strips).

3. Charge pulses in drift strip detectors

The complex strip electrode structure and the effects of physical processes occurring in CZT detectors (charge sharing, charge trapping) give rise to various charge pulses with different features and shapes. In this section, we present an overview of the charge pulses generated in CZT drift strip detectors, with the goal to better understand, through simulations and measurements, the nature of these pulses and their role in detector performance. This is very important for a proper setting of the pulse processing analysis and the development of new strategies for spectroscopic and spatial performance improvements. Generally, the generation of pulses in CZT detectors can be clearly explained through the Shockley–Ramo theorem (He *et al.*, 2001; Knoll, 2000; Ramo, 1939; Shockley, 1938) with the concept of weighting potential. The charge generated on an electrode is related to the variation of the weighting potential between the charge generation and collection points. The presence of monotonic and non-

Figure 3
Layout of a single drift cell of the 3D drift strip CZT detectors. Each drift cell (1.6 mm × 6 mm × 20 mm) contains a collecting anode strip and four drift strips, two RDs and two LDs of the collecting strip. The bias voltage values are optimized to collect electron charges on the collecting anode. The PTF and PPF irradiation geometries are also shown.

Monte Carlo methods (*Geant4*) (Agostinelli *et al.*, 2003), (ii) electric and weighting field calculation by the finite element method (FEM) with COMSOL Multiphysics and (iii) calculation of the charge carrier transport and pulse formation in a MATLAB environment (Bettelli *et al.*, 2020). The charge carrier transport properties used in the simulation are typical of Redlen CZT materials for low-flux applications (LF-CZT materials): μ_e of 1100 cm^2 V^{-1} s^{-1} and τ_e of 11 μs for electrons and μ_h of 88 cm^2 V^{-1} s^{-1} and τ_h of 0.2 μs for holes (Thomas *et al.*, 2017).

Fig. 4 shows an overview of simulated and measured pulses from the anode, cathode and drift strips (electrode voltages: −350 V for the cathodes, −200 V for the central drift strips and −100 V for the adjacent drift strips). Photon interactions near the cathode (top) and the anode (bottom) are mainly focused (the black circular points represent the photon interaction positions). For each photon interaction, the measured pulses are detected in temporal coincidence. Both simulations and measurements produce similar results on the key features of the pulses.

monotonic weighting potentials often creates pulses with different shapes, strongly dependent on the charge carrier generation positions and trajectories. Generally, the detector pulses can be classified as 'collected-charge' and 'induced-charge' pulses. The collected-charge pulses are generated by charge carriers that are in fact collected by an electrode (collecting electrode), whereas the induced-charge pulses on a non-collecting electrode are generated by charge carriers collected by another electrode. The movement of charge carriers in the vicinity of the collecting electrode can induce a small charge on the surrounding non-collecting electrodes. This effect is known as 'weighting potential cross talk' (Guerra *et al.*, 2008; Brambilla *et al.*, 2012) and the induced-charge pulses are also called transient pulses (Bolotnikov *et al.*, 2016; Kim *et al.*, 2011). Ideally, the induced-charge pulses should have bipolar amplitude and should saturate to a zero-level (baseline), highlighting that no charge is collected by the electrode. In real detectors, owing to the presence of charge sharing and charge trapping, the induced-charge pulses often saturate to a non-zero level; moreover, the pulse shapes can simultaneously contain components caused by charge collection and weighting potential cross talk (Bolotnikov *et al.*, 2014).

The wide variety of collected and induced-charge pulses in CZT drift strip detectors is mainly represented by the following pulse classes: (i) collected-charge pulses, (ii) induced-charge pulses with zero-saturation level, (iii) induced-charge pulses with negative and positive saturation levels.

The measured pulses (*i.e.* the output pulses from charge sensitive preamplifiers) are the result of photoelectric interactions of 662 keV photons from a ^{137}Cs source. The simulated pulses come from a custom procedure organized into three main blocks: (i) radiation–semiconductor interaction with

points represent the photon interaction positions). For each photon interaction, the measured pulses are detected in temporal coincidence. Both simulations and measurements produce similar results on the key features of the pulses.

3.1. Collected-charge pulses

Positive and negative collected-charge pulses are typically created by anode and cathode strips, respectively. As shown in Fig. 4, the weighting potential of the anode strips, similarly to pixel detectors (Abbene *et al.*, 2018*a*; Barrett *et al.*, 1995), is shrunk near the anode, thus reducing the contribution of the holes in the charge pulses (single-electron charge sensing pulses). However, as also observed in pixel detectors, single-electron charge sensing is reduced for photon interactions near the anode. The shape of collecting anode pulses (positive light-blue pulses of Fig. 4) strongly depends on the charge generation point (photon interaction). For photon interactions near the cathode (top side of Fig. 4), the anode pulses are characterized by a leading edge with slow and fast slopes, following the behaviour of the anode weighting potential; however, near the anode (bottom side of Fig. 4), only a fast slope features the leading edge. In particular, the presence of the slow leading edge represents a critical issue on the estimation of the arrival time of the events.

Due to a coarse strip segmentation, the weighting potential of the cathode strips spans between the cathode and anode electrodes, producing charge pulses more sensitive to the hole contribution. Contrary to the anode pulses, the collected-charge pulses from cathode strips have a well defined slope of the leading edge (negative blue pulses of Fig. 4), with benefits in arrival time estimation. The peaking times of the pulses can reach maximum values of 2 μs and 3 μs for the anode and
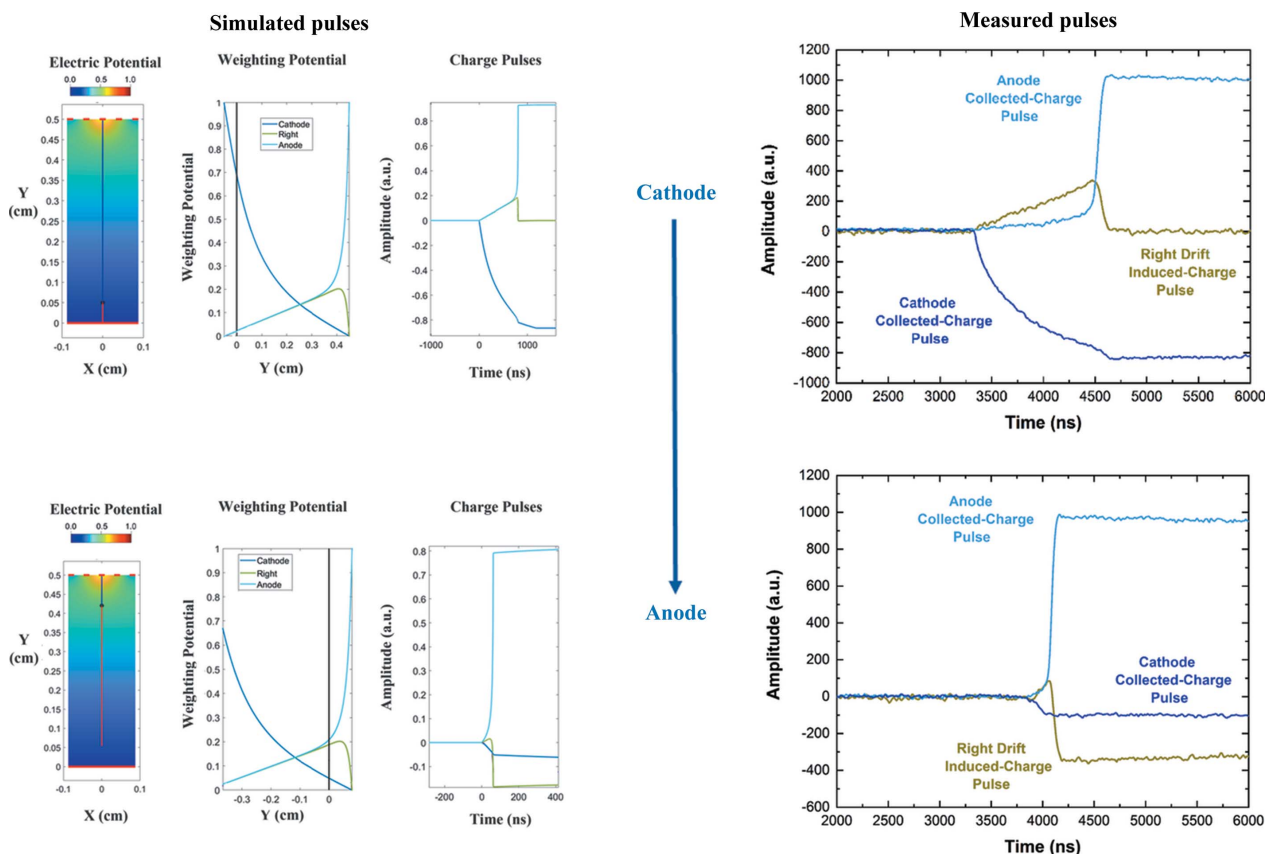
Figure 4
Measured and simulated pulses from the anode, cathode and drift strips. Calculated electric and weighting potential profiles are also reported. Collected and induced-charge pulses are clearly visible, related to photon interaction near the cathode (top) and near the anode (bottom).

cathode, respectively. This indicates that a long shaping time constant of the shaper amplifier is required to avoid ballistic deficit distortions (Knoll, 2000).

3.2. Induced-charge pulses with zero-saturation level

Positive induced-charge pulses (dark-yellow pulses) with zero-saturation level are observed in drift strips, as shown on the top side of Fig. 4. These pulses are mainly caused by photon interactions near the cathode and are related to the electron charge drift: the electron charge, drifting towards the anode, also intercepts the non-monotonic weighting potential of the drift strips (dark-yellow curve). The pulses rise as the electron charge moves to the collecting anode and then rapidly decrease to zero as the electrons are collected. Their amplitude (pulse height) can be used to estimate the photon interaction positions among the anode/drift strips (x-positioning) (Howalt Owe *et al.*, 2019; Budtz-Jørgensen & Kuvvetli, 2017). These pulses are also observed in cathode strips and can be helpful to improve z-positioning among the cathodes, with spatial resolution better than the geometrical strip pitch (2 mm).

3.3. Induced-charge pulses with positive- and negative-saturation levels

Induced-charge pulses with a negative saturation level are also characteristic of drift strips, particularly for photon

interactions near the anode, as shown in the bottom side of Fig. 4. This negative saturation level is due to the charge induced by holes trapped in the detector (Bolotnikov *et al.*, 2014, 2016; Zhu *et al.*, 2011), as also confirmed by our simulation. Since the amplitude of this negative level is related to hole trapping, this information can be used to reduce the effects of incomplete charge collection in the collected-charge pulses of the anode strips, detected in temporal coincidence.

The drift strips also give rise to induced-charge pulses with positive saturation levels (Fig. 5). These pulses, mainly related to photon interactions near the cathode, are caused by the charge induced by electrons trapped in the detector. Due to the moderate trapping of electrons, the number of these pulses is very low when compared with that of the holes. Fig. 5 also shows the presence of three different cathode pulses that can be attributed to the effects of charge sharing among cathode strips. If a ^{137}Cs photon is fully absorbed near the cathode side of the CZT detector, the size (FWHM) of the electron cloud, after drifting through the entire thickness of the crystal, can be estimated to about 350 µm (range of the photoelectrons, diffusion and repulsion) (Bettelli *et al.*, 2020; Kim *et al.*, 2011, 2014; Bolotnikov *et al.*, 2007). In particular, the pulse from cathode 7 (brown pulse) is an example of mixed induced-collected-charge pulses, owing to the effects of both charge sharing and weighting potential cross talk. Fortunately, due to the focusing effects of the drift strips, these pulses are not present in collecting anode strips. Mixed induced-collected-
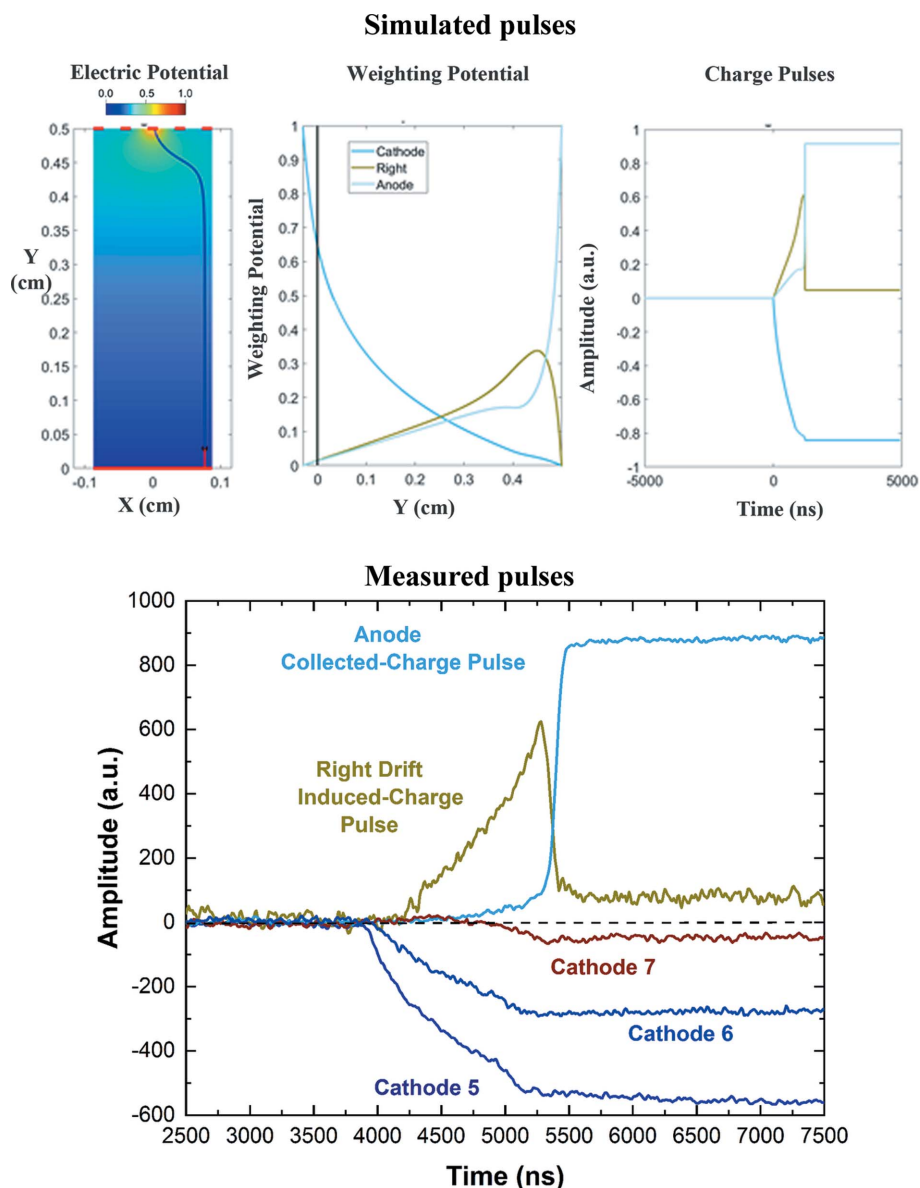
Simulated pulses

Measured pulses

Figure 5
Simulated and measured pulses from the anode, cathode and drift strips. Induced-charge pulses with positive saturation levels can be attributed to the electron trapping. Mixed induced-collected charge pulses (cathode 7) are also observed, due to both charge sharing and weighting potential cross talk.

Italy; http://www.caen.it) driven by an original firmware (Abbene *et al.*, 2015, Abbene & Gerardi, 2015; Gerardi & Abbene, 2014). The data from each channel are transmitted through USB to PCs, where the user can control both the acquisition and the analysis. Due to the complex analysis required by the different pulse shapes, we performed, at this step, a mixed online/offline pulse processing. For each CSP output channel, the digital system performs online pulse detection, time-tag triggering and provides to the PCs a sequence of selected pulses with the related arrival times ('snapshot waveform'); therefore, these pulses are analysed offline for dedicated pulse shape and height analysis. The details of online operations and outputs from each CSP output channel are described below:

(i) Pulse detection and arrival time estimation: the CSP output waveforms are shaped using the classical single delay line (SDL) shaping technique (Knoll, 2000), acting as the classical differentiation; the trigger time is generated and time-stamped through the ARC (amplitude and rise time compensation) timing marker (at the leading edge of the SDL pulses), able to reduce the effects of time jitters and amplitude and rise time walks.

(ii) Snapshot waveforms (SWs): a sequence of CSP output pulses with the related arrival times are provided to PCs (Fig. 6) for the offline pulse shape and height analysis; each CSP pulse, selected through a pile-up rejection (PUR), is centred on a time window, the duration of which is termed 'snapshot time' (ST); a pulse is accepted if it is not preceded and not followed by another pulse in the ST/2 time windows.

charge pulses generally have a strong presence in pixel detectors (Bolotnikov *et al.*, 2014, 2016), representing a critical issue in the estimation of pulse heights (photon energies).

4. The electronics: preamplifiers and digital electronics

The collecting anode strips, the drift strips and the cathode strips were a.c.-coupled to hybrid charge-sensitive preamplifiers (CSPs) and processed by 32-channel digital electronics. Both the CSPs and the digital electronics were developed at DiFC of the University of Palermo (Italy). The CSPs are characterized by an equivalent noise charge (ENC) of 100 electrons and equipped with a resistive-feedback circuit with a decay time constant of 150 µs. The digital electronics consists of eight digitizers (DT5724, 16 bit, 100 MS s^{-1}, CAEN S.p.A.,

We stress that SWs are quite different from the classical waveforms of a digitizer; this operation mode allows dedicated analysis of the pulses and, due to the estimation of the arrival times, enables the possibility of time coincidence analysis (TCA) with the preservation of the pulse shape. Moreover, each SW is characterized by the absence of empty waveform zones, *i.e.* with no pulses. On the contrary, empty zones are typically present in the classical waveforms, especially at low-input counting rates, requiring larger output files and, therefore, with critical issues in synchronization and data transmission.

The SWs are processed offline with dedicated analysis taking into account the different features of collected-charge
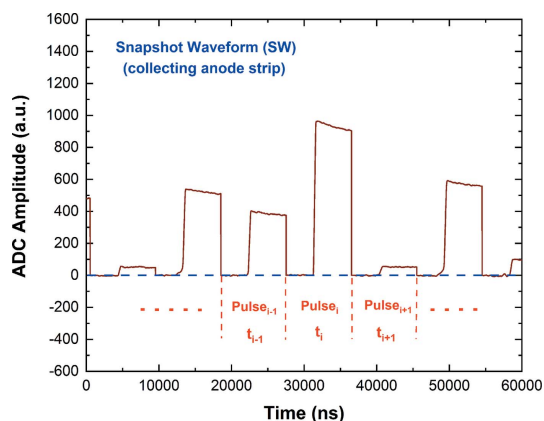
Figure 6
Overview of an SW from a single channel (collecting anode strip) of the digital readout electronics. Each CSP output pulse, detected online, is given within a user-selected time window of 9 μs (ST) and time-tagged with its arrival time. The SWs are transmitted to PCs for dedicated offline pulse processing.
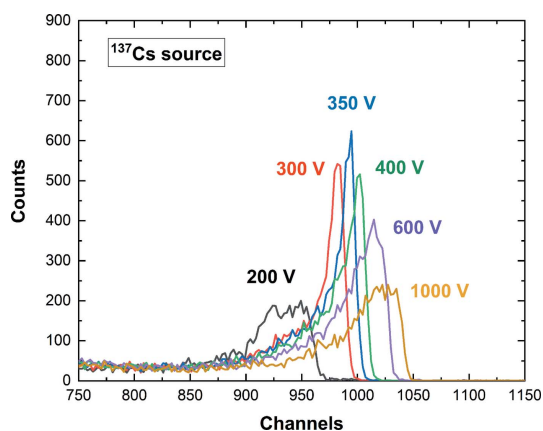

Figure 7
662 keV photopeaks of the measured ^{137}Cs spectra from a collecting anode strip at different cathode bias voltages; fixed drift strip voltages (adjacent drift strips: −100 V; central drift strips: −200 V) are used. The detector, irradiated in PTF geometry, shows the best energy resolution (1.3% FHWM at 661.7 keV) at a cathode voltage of −350 V (583 V cm^{-1}).

pulses and induced-charge pulses. The height (*i.e.* the photon energy), the saturation levels (contribution induced by trapped charges) and the peaking time (*i.e.* the pulse shape) of the pulses are estimated offline after SDL and trapezoidal shaping.

5. Experimental

The spectroscopic response of the detectors was investigated by X-ray and gamma-ray calibration sources (main gamma lines: ^{241}Am, 59.5 keV and 26.3 keV; ^{57}Co, 122.1 keV and 136.5 keV; ^{137}Cs: 661.7 keV). The 3D working mode of the detectors foresees the PTF irradiation geometry (*xy* plane), exploiting the 20 mm thickness of the CZT material in the *z* direction. For comparison, the spectroscopic performance through the PPF geometry (*zx* plane) was also evaluated. All measurements were performed at $T = 25°C$.

6. Overview of the spectroscopic performance

Fig. 7 shows the measured 662 keV photopeaks of uncollimated ^{137}Cs spectra for a collecting anode strip at different cathode bias voltages. The drift strip bias voltages of −100 V for adjacent drift strips and −200 V for central drift strips represent the best compromise between charge collection improvements and leakage current increasing. The results clearly highlight that the best energy resolution was obtained at low cathode voltage values (−350 V; 583 V cm^{-1}). This is due to the particular electrode structure of the detector: once the drift strip voltages are fixed, higher cathode voltages worsen the electron charge collection on the collecting anode, as confirmed through simulations (Fig. 8). We obtained spectra with excellent energy resolution of 1.3% FWHM at 661.7 keV without any corrections for charge sharing or trapping. This is a key result, confirming the important technological progress obtained in the fabrication of CZT drift strip detectors. Typically, energy resolutions of 3–4% at 662 keV were obtained from uncollimated raw ^{137}Cs spectra measured with
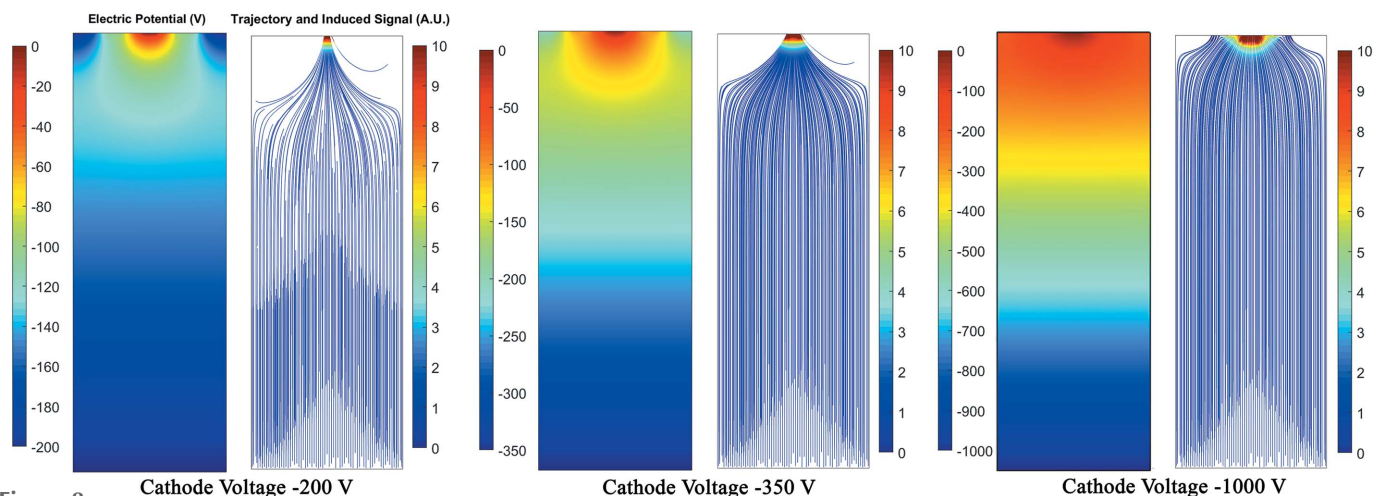

Figure 8
Calculated electric potential and simulated electron induced current at different cathode voltages (adjacent drift strips: −100 V; central drift strips: −200 V). The results clearly show that the induced current on the collecting anode strip is enhanced at −350 V.

other CZT drift strip prototypes (Budtz-Jørgensen & Kuvvetli, 2017; Howalt Owe *et al.*, 2019; Kalemci & Matteson, 2002; Kuvvetli *et al.*, 2010). Fig. 9 shows uncollimated ^{57}Co spectra measured using the PTF and PPF geometries. At low energies (^{241}Am and ^{57}Co sources), the PPF geometry ensures better performance than that of PTF due to charge generation near the cathode side. In this case the pulses are less sensitive to the hole contribution. However, at higher energies (^{137}Cs source), with charge generation points spanning the overall cathode to anode depth, similar performance characterizes the two irradiation geometries, as reported in Table 1. In this case, the PTF geometry will ensure higher detection efficiency over the 20 mm thickness.

7. Spectroscopic improvements with cathode signals (C/A ratio, cathode peaking time, electron drift time)

A critical issue observed in 3D CZT drift strip detectors is represented by the presence of non-uniform spectroscopic response over the cathode–anode depth, with increasing degradations for photon interactions near the anode (Budtz-Jørgensen & Kuvvetli, 2017; Howalt Owe *et al.*, 2019). Regarding our detectors, evidence of the presence of these distortions was given by the differences observed in detector performance between PTF and PPF geometries, as shown in the previous section. These distortions are better highlighted by the measured spectra (Fig. 10) from collimated ^{57}Co photon beams (Pb collimator; circular hole diameter $\phi = 1$ mm) irradiated in PTF geometry at three different positions between the cathode and anode. The photopeak centroid is reduced by about 6% from the cathode to the anode and the energy
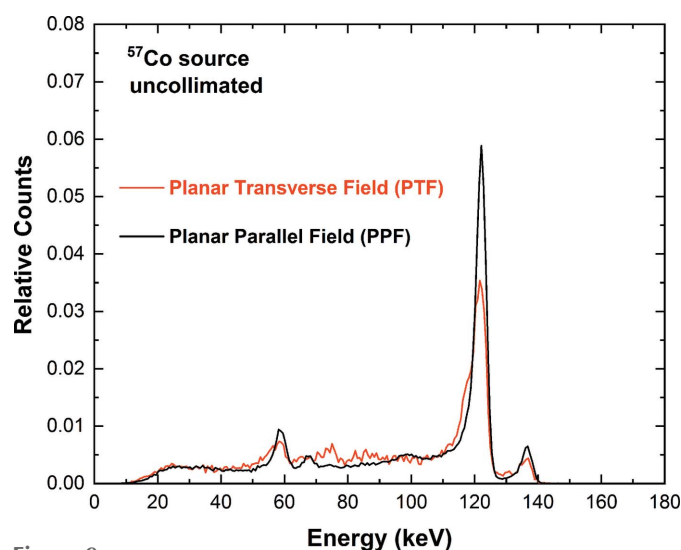
Table 1
Energy resolution (FWHM) at different energies of a collecting anode strip of the 3D CZT drift strip detector in PTF and PPF geometries.

The energy resolution values refer to raw energy spectra with no spectral correction. The Fano noise was calculated using a Fano factor of $F = 0.1$ (Devanathan *et al.*, 2006; Kuvvetli & Budtz-Jorgensen, 2005; Owens & Peacock, 2004).

Irradiation geometry	Energy resolution at 59.5 keV (keV) Fano noise: 0.4 keV	Energy resolution at 122.1 keV (keV) Fano noise: 0.6 keV	Energy resolution at 661.7 keV (keV) Fano noise: 1.3 keV
Planar transverse field	4.2 (7%)	6.0 (4.9%)	8.6 (1.3%)
Planar parallel field	3.3 (5.6%)	4.0 (3.3%)	7.9 (1.2%)

resolution worsens from 3.2% (near the cathode) to 7.5% (near the anode) FWHM at 122.1 keV. This is due to the fact that the weighting potential behaviour of the collecting anode near the anode increases the sensitivity of the pulses to the hole contribution and hence to their trapping effects. In general, mitigation of these non-uniformities can be obtained through the analysis of some features of the cathode and anode pulses. In our case the cathode to anode (C/A) ratio, the cathode peaking time and the electron drift time were estimated with the goal to exploit their potential in performance recovery. As is well known (Bolotnikov *et al.*, 2016; Kim *et al.*, 2014; Budtz-Jørgensen & Kuvvetli, 2017; Van Pamelen *et al.*, 1998; Verger *et al.*, 2007; Yi *et al.*, 2013), the C/A ratio is widely used in CZT detectors to compensate for these distortions. However, some critical issues must be taken into account when the C/A ratio is used in CZT drift strip detectors. First, owing to the low cathode bias voltages (-350 V), the energy spectra from the cathode strips are very poor [Fig. 11(*a*)]. This creates significant fluctuations in C/A ratio values and problems in energy calibration of the cathodes. Here, the cathode calibration was successfully performed through low-energy spectra (^{241}Am and ^{57}Co sources) measured in PPF

Figure 9
Measured ^{57}Co spectra of a collecting anode strip in PTF and PPF geometries. Energy resolution of 4.9% and 3.3% FWHM at 122.1 keV were obtained in PTF and PPF geometries, respectively.
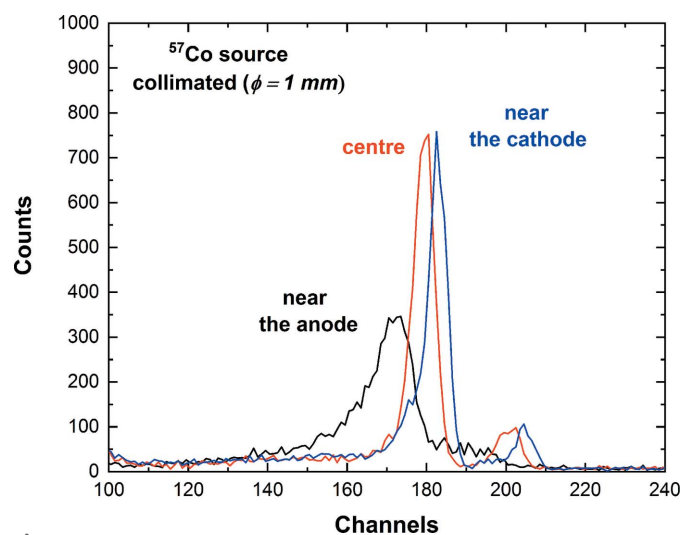

Figure 10
Collimated ($\phi = 1$ mm) ^{57}Co spectra of a collecting anode strip in PTF geometry at different irradiation positions. The energy spectra show photopeak centroid shifts of about 6% from the cathode to the anode side; the energy resolution is 3.2% and 7.5% FWHM at 122.1 keV near the cathode and anode, respectively.
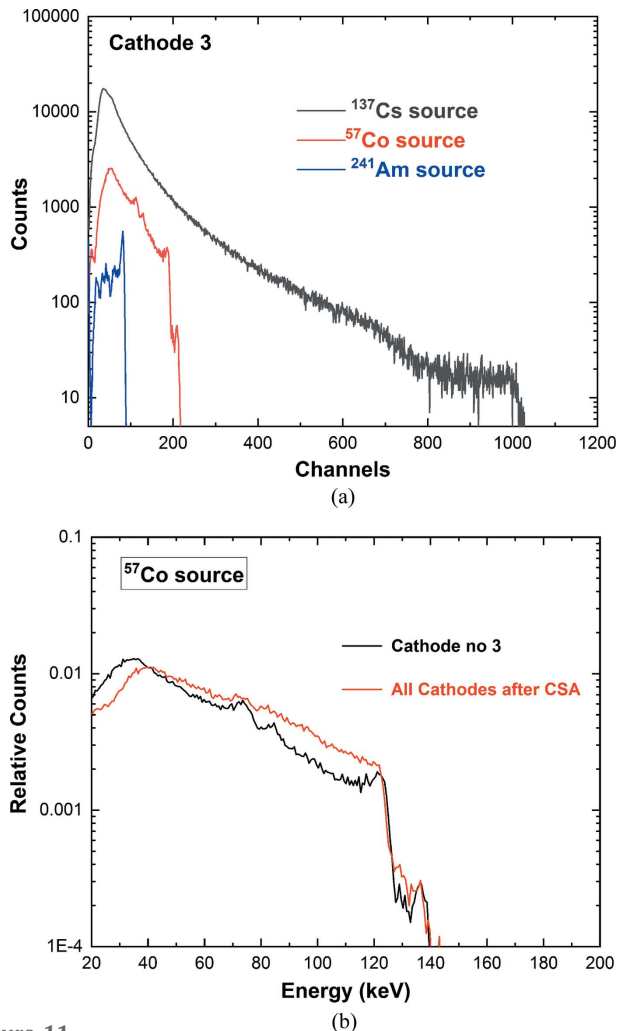
Figure 11
(a) Measured energy spectra from a cathode strip (PTF geometry).
(b) ^{57}Co energy spectrum (red line) of all cathode strips after CSA.

geometry, obtaining quite good linearity. Second, charge sharing is present among the cathode strips (Fig. 5) and, therefore, charge sharing addition (CSA) is necessary to correctly estimate the total charge from the cathode strips. As previously demonstrated (Abbene *et al.*, 2018*b*; Allwork *et al.*, 2012; Brambilla *et al.*, 2012; Bolotnikov *et al.*, 1999; Gaskin *et al.*, 2003; Kalemci & Matteson, 2002; Kim *et al.*, 2011), CSA simply consists of a sum of the energies of the coincidence events among the collecting electrodes (cathode strips in our detectors). Fig. 11(*b*) shows the ^{57}Co spectra from a cathode strip (cathode 3) and from all cathodes after CSA [red line of Fig. 11(*b*)]. Due to the small inter-strip gap (0.1 mm), if compared with the strip pitch (2 mm), no charge losses are observed after CSA. The peaking time of the cathode pulses also follows the depth of interaction between the cathode and anode; due to the similar peaking time values of the shared pulses, it can be helpful when CSA fails. The electron drift time is the time between the charge generation of the electron cloud until its collection at the anode strip. This is very helpful for double-event positioning of Compton interactions (Compton camera). The estimation of the drift time is strongly

influenced by the correct measurement of the arrival times of the pulses which is more critical for the anode pulses due to their slow leading edge for photon interactions near the cathode. In our case, to take this into account, we estimated the electron drift time T_{drift} using the following approach,

$$T_{\text{drift}} = \begin{cases} T_{\text{anode}} - T_{\text{cathode}} + T_{\text{anode peaking time}} & \text{if } T_{\text{anode}} > T_{\text{cathode}} \\ T_{\text{anode peaking time}} & \text{if } T_{\text{anode}} \leq T_{\text{cathode}} \end{cases}$$
(1)

where T_{anode} and T_{cathode} are the arrival times of the anode and cathode strip pulses, respectively, and $T_{\text{anode peaking time}}$ is the peaking time of the anode pulses.

Fig. 12 shows the scatter plots, zoomed in on the 662 keV photopeak region, of the measured C/A ratio, the cathode peaking time and the electron drift time versus the height of the pulses from a collecting anode strip. Photopeak shifts, mainly related to interactions near the anode, are visible at low values of these features. The curvature at high C/A values (C/A > 0.7) also confirms the presence of a small contribution from the electron trapping for photon interactions near the cathode. The scatter plot related to the cathode peaking time is more smeared out. This is probably due to the presence of two opposite tendencies in the values of cathode peaking time; one is related to the holes that tend to increase the cathode peaking time near the anode, another to the electrons which tend to reduce this value. Through the measured scatter plots, we approached a possible performance recovery. In particular, the corrected anode energy E_{corr} is obtained as follows:

$$E_{\text{corr}} = E_{\text{meas}}(F) \frac{E_{\text{best photopeak}}}{E_{\text{photopeak}}(F)},$$
(2)

where F is the measured feature (C/A, cathode peaking time or drift time), $E_{\text{meas}}(F)$ is the measured raw energy, $E_{\text{best photopeak}}$ is the best photopeak energy (estimated from the energy spectra measured in PPF geometry) and $E_{\text{photopeak}}(F)$ is the photopeak of the energy spectrum associated with the feature F. The ^{137}Cs energy spectra after spectral correction (C/A and drift time) using equation (2) are shown in Fig. 13. In general, the C/A correction gives a slightly better energy resolution (1% FWHM at 661.7 keV) than that of the drift time (1.16% FWHM at 661.7 keV). However, C/A correction requires the rejection of some C/A ratio values which give poor results [blue line of Fig. 13(*a*)], while drift time correction allows the analysis of all events.

8. Spectroscopic improvements with drift strip signals

In previous sections, we presented some induced-charge pulses from drift strips characterized by negative saturation levels. Through simulation, we also demonstrated that this saturation level is due to the charge induced by trapped holes, opening the possibility to use this feature to reduce the effects of incomplete charge collection. Fig. 14(*a*) shows the scatter plot, zoomed in on the 662 keV photopeak region, of the negative saturation level versus the height of the pulses from a collecting anode strip. Photopeak lowering is increased for
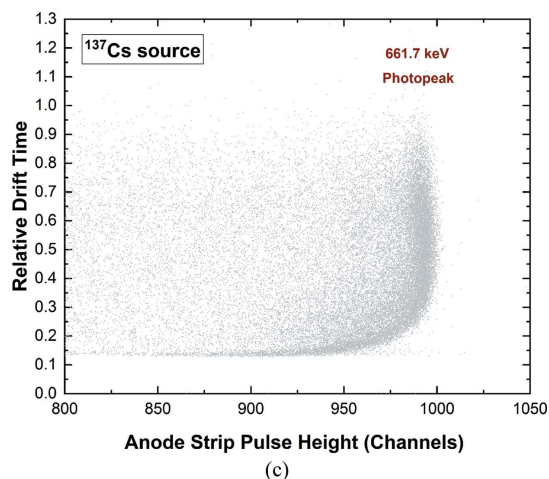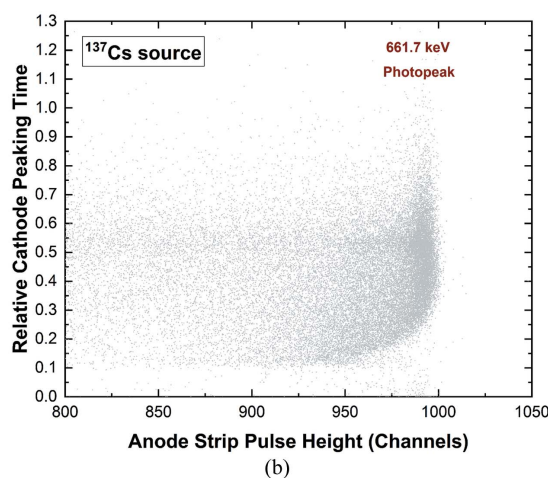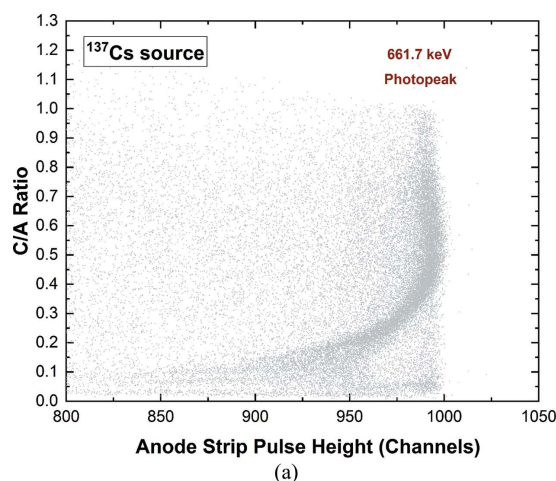
Figure 12
Scatter plots of (*a*) the C/A ratio, (*b*) the relative cathode peaking time and (*c*) the relative drift time versus the height of the pulses from a collecting anode strip.

higher negative saturation levels. By employing equation (2) with this new feature *F* (*i.e.* the negative saturation level), we obtained a full photopeak recovery [Fig. 14(*b*)] and significant improvements in the energy spectra (0.8% FWHM at 661.7 keV), as shown in Fig. 14(*c*). The ^{137}Cs energy spectrum with the collecting anode strip events in temporal coincidence with all events from drift and cathode strips is shown in Fig. 15.
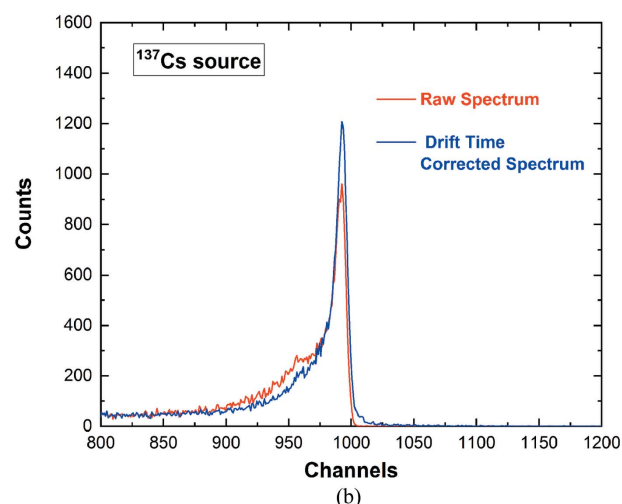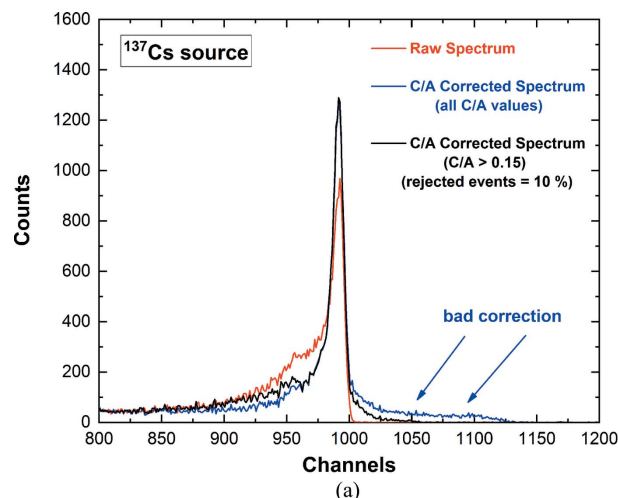

Figure 13
Measured ^{137}Cs energy spectra corrected with equation (2). (*a*) C/A ratio correction (black and blue lines). (*b*) Drift time correction (blue line). Energy resolutions of 1% and 1.16% FWHM at 661.7 keV are obtained for the C/A ratio and drift time correction, respectively.

The correction was only applied to the anode strip pulses in temporal coincidence with the induced-charge pulses with negative saturation levels. An excellent energy resolution of 0.9% FWHM at 661.7 keV characterizes the measured spectrum. To the best of our knowledge, this result represents the best energy resolution value obtained with 3D CZT drift detectors (Budtz-Jørgensen & Kuvvetli, 2017; Caroli *et al.*, 2010; Howalt Owe *et al.*, 2019; Kalemci & Matteson, 2002; Kuvvetli *et al.*, 2010).

9. Conclusions

The spectroscopic performance of new high-resolution 3D CZT drift strip detectors (19.4 mm × 19.4 mm × 6 mm) is presented. The detectors are designed to ensure room-temperature measurement of photon energy, timing and 3D positioning up to the megaelectronvolt region, with a moderate number of readout channels (24) for each detector. Due to the focusing effects of the drift strips, charge sharing and mixed induced-collected-charge pulses are not present in
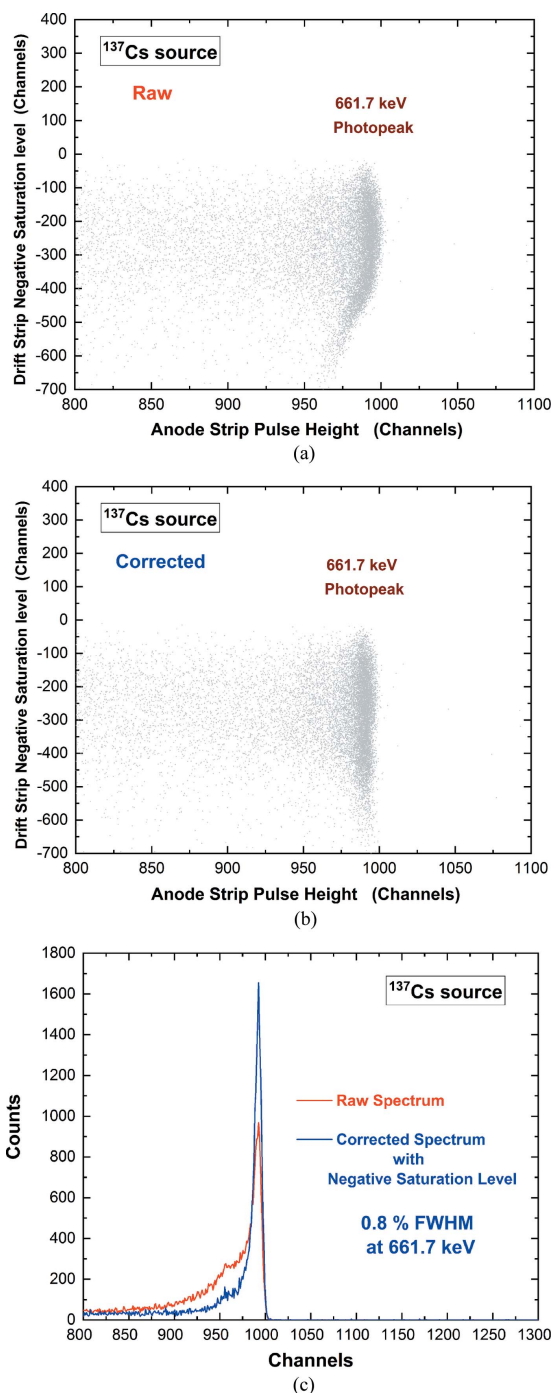
Figure 15
Measured uncollimated ^{137}Cs energy spectrum from a collecting anode strip after spectral correction. The energy spectrum is obtained with the collecting anode strip events in temporal coincidence with all pulses from drift and cathode strips. The correction was only applied to the anode strip pulses in temporal coincidence with the induced-charge pulses with negative saturation levels.

Italy). Dedicated digital pulse processing, developed at the University of Palermo (Italy), allowed us to exploit the features of the wide range of collected and induced charge pulses from the strips, with excellent results in detector performance enhancements. In particular, the non-uniformities over the cathode–anode depth, typically present in CZT drift strip detectors, were recovered through the relation of the anode pulses with the C/A ratio, cathode peaking time and drift time (1.0–1.16% FWHM at 661.7 keV). Excellent spectroscopic improvements (0.8–0.9% FWHM at 661.7 keV) were obtained with a new approach, based on the relation of the anode strip pulses with negative saturation levels of the induced-charge pulses from the drift strips.

Ongoing activities involve the full characterization of the spatial capabilities of the detectors in 3D event reconstruction. Future work will focus on the capabilities of 3D CZT drift strip detectors as Compton cameras.

References

Abbaszadeh, S., Gu, Y., Reynolds, P. D. & Levin, C. S. (2016). *Phys. Med. Biol.* **61**, 6733–6753.
Abbene, L., Del Sordo, S., Fauci, F., Gerardi, G., La Manna, A., Raso, G., Cola, A., Perillo, E., Raulo, A., Gostilo, V. & Stumbo, S. (2007). *Nucl. Instrum. Methods Phys. Res. A*, **583**, 324–331.
Abbene, L. & Gerardi, G. (2015). *J. Synchrotron Rad.* **22**, 1190–1201.
Abbene, L., Gerardi, G. & Principato, F. (2013*b*). *Nucl. Instrum. Methods Phys. Res. A*, **730**, 124–128.
Abbene, L., Gerardi, G. & Principato, F. (2015). *Nucl. Instrum. Methods Phys. Res. A*, **777**, 54–62.

Figure 14
(*a*) Raw and (*b*) corrected [equation (2)] scatter plots of the negative saturation level versus the height of pulses from a collecting anode strip. (*c*) Excellent energy resolution is obtained after correction considering only the induced-charge pulses with negative saturation level.

collecting anode strips. As reported in the literature, mixed induced-collected-charge pulses have a strong presence in pixelated CZT detectors, representing a critical issue in the correct estimation of the pulse heights. Very good room-temperature energy resolution (1.3% FWHM at 661.7 keV) of the raw energy spectra (with no correction) demonstrates the important advances in device fabrication technology obtained at IMEM/CNR (Parma, Italy) and by due2lab (Reggio Emilia,
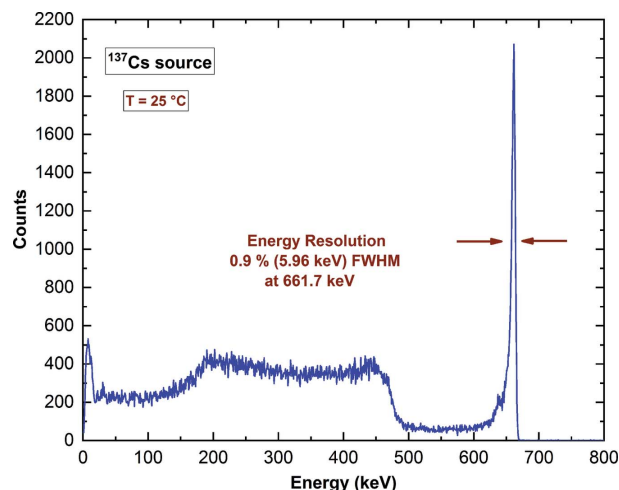
Abbene, L., Gerardi, G., Principato, F., Bettelli, M., Seller, P., Veale, M. C., Fox, O., Sawhney, K., Zambelli, N., Benassi, G. & Zappettini, A. (2018*b*). *J. Synchrotron Rad.* **25**, 1078–1092.

Abbene, L., Gerardi, G., Raso, G., Basile, S., Brai, M. & Principato, F. (2013*a*). *J. Instrum.* **8**, P07019.

Abbene, L., Gerardi, G., Turturici, A. A., Raso, G., Benassi, G., Bettelli, M., Zambelli, N., Zappettini, A. & Principato, F. (2016). *Nucl. Instrum. Methods Phys. Res. A*, **835**, 1–12.

Abbene, L., Principato, F., Gerardi, G., Bettelli, M., Seller, P., Veale, M. C., Zambelli, N., Benassi, G. & Zappettini, A. (2018*a*). *J. Synchrotron Rad.* **25**, 257–271.

Abbene, L., Principato, F., Gerardi, G., Buttacavoli, A., Cascio, D., Bettelli, M., Amadè, N. S., Seller, P., Veale, M. C., Fox, O., Sawhney, K., Zanettini, S., Tomarchio, E. & Zappettini, A. (2020). *J. Synchrotron Rad.* **27**, 319–328.

Agostinelli, S., Allison, J., Amako, K., Apostolakis, J., Araujo, H., Arce, P., Asai, M., Axen, D., Banerjee, S., Barrand, G., Behner, F., Bellagamba, L., Boudreau, J., Broglia, L., Brunengo, A., Burkhardt, H., Chauvie, S., Chuma, J., Chytracek, R., Cooperman, G., Cosmo, G., Degtyarenko, P., Dell'Acqua, A., Depaola, G., Dietrich, D., Enami, R., Feliciello, A., Ferguson, C., Fesefeldt, H., Folger, G., Foppiano, F., Forti, A., Garelli, S., Giani, S., Giannitrapani, R., Gibin, D., Gómez Cadenas, J. J., González, I., Gracia Abril, G., Greeniaus, G., Greiner, W., Grichine, V., Grossheim, A., Guatelli, S., Gumplinger, P., Hamatsu, R., Hashimoto, K., Hasui, H., Heikkinen, A., Howard, A., Ivanchenko, V., Johnson, A., Jones, F. W., Kallenbach, J., Kanaya, N., Kawabata, M., Kawabata, Y., Kawaguti, M., Kelner, S., Kent, P., Kimura, A., Kodama, T., Kokoulin, R., Kossov, M., Kurashige, H., Lamanna, E., Lampén, T., Lara, V., Lefebure, V., Lei, F., Liendl, M., Lockman, W., Longo, F., Magni, S., Maire, M., Medernach, E., Minamimoto, K., Mora de Freitas, P., Morita, Y., Murakami, K., Nagamatu, M., Nartallo, R., Nieminen, P., Nishimura, T., Ohtsubo, K., Okamura, M., O'Neale, S., Oohata, Y., Paech, K., Perl, J., Pfeiffer, A., Pia, M. G., Ranjard, F., Rybin, A., Sadilov, S., Di Salvo, E., Santin, G., Sasaki, T., Savvas, N., Sawada, Y., Scherer, S., Sei, S., Sirotenko, V., Smith, D., Starkov, N., Stoecker, H., Sulkimo, J., Takahata, M., Tanaka, S., Tcherniaev, E., Safai Tehrani, E., Tropeano, M., Truscott, P., Uno, H., Urban, L., Urban, P., Verderi, M., Walkden, A., Wander, W., Weber, H., Wellisch, J. P., Wenaus, T., Williams, D. C., Wright, D., Yamada, T., Yoshida, H. & Zschiesche, D. (2003). *Nucl. Instrum. Methods Phys. Res. A*, **506**, 250–303.

Allwork, C., Kitou, D., Chaudhuri, S., Sellin, P. J., Seller, P., Veale, M. C., Tartoni, N. & Veeramani, P. (2012). *IEEE Trans. Nucl. Sci.* **59**, 1563–1568.

Alruhaili, A., Sellin, P. J., Lohstroh, A., Veeramani, P., Kazemi, S., Veale, M. C., Sawhney, K. J. S. & Kachkanov, V. (2014). *J. Instrum.* **9**, C03029.

Barret, H. H., Eskin, J. D. & Barber, H. B. (1995). *Phys. Rev. Lett.* **75**, 156–159.

Benassi, G., Nasi, L., Bettelli, M., Zambelli, N., Calestani, D. & Zappettini, A. (2017). *J. Instrum.* **12**, P02018.

Bettelli, M., Amadè, N. S., Calestani, D., Garavelli, B., Pozzi, P., Macera, D., Zanotti, L., Gonano, C. A., Veale, M. C. & Zappettini, A. (2020). *Nucl. Instrum. Methods Phys. Res. A*, **960**, 163663.

Bolotnikov, A. E., Bale, D., Butcher, J., Camarda, G. S., Cui, Y., De Geronimo, G., Fried, J., Hossain, A., Kim, K. H., Marshall, M., Soldner, S., Petryk, M., Prokesch, M., Vernon, E., Yang, G. & James, R. B. (2014). *IEEE Trans. Nucl. Sci.* **61**, 787–792.

Bolotnikov, A. E., Camarda, G. S., Carini, G. A., Cui, Y., Li, L. & James, R. B. (2007). *Nucl. Instrum. Methods Phys. Res. A*, **571**, 687–698.

Bolotnikov, A. E., Camarda, G. S., Cui, Y., De Geronimo, G., Eger, J., Emerick, A., Fried, J., Hossain, A., Roy, U., Salwen, C., Soldner, S., Vernon, E., Yang, G. & James, R. B. (2016). *Nucl. Instrum. Methods Phys. Res. A*, **805**, 41–54.

Bolotnikov, A. E., Camarda, G. S., Geronimo, G. D., Fried, J., Hodges, D., Hossain, A., Kim, K., Mahler, G., Giraldo, L. O., Vernon, E.,

Yang, G. & James, R. B. (2020). *Nucl. Instrum. Methods Phys. Res. A*, **954**, 161036.

Bolotnikov, A. E., Cook, W. R., Harrison, F. A., Wong, A., Schindler, S. M. & Eichelberger, A. C. (1999). *Nucl. Instrum. Methods Phys. Res. A*, **432**, 326–331.

Brambilla, A., Ouvrier-Buffet, P., Rinkel, J., Gonon, G., Boudou, C. & Verger, L. (2012). *IEEE Trans. Nucl. Sci.* **59**, 1552–1558.

Budtz-Jørgensen, C. & Kuvvetli, I. (2017). *IEEE Trans. Nucl. Sci.* **64**, 1611–1618.

Butler, J. F., Lingren, C. L. & Doty, F. P. (1992). *IEEE Trans. Nucl. Sci.* **39**, 605–609.

Caroli, E., Auricchio, N., Del Sordo, S., Abbene, L., Budtz-Jørgensen, C., Casini, F., da Silva, R. M. C., Kuvvetlli, I., Milano, L., Natalucci, L., Quadrini, E. M., Stephen, J. B., Ubertini, P., Zanichelli, M. & Zappettini, A. (2010). *Proc. SPIE*, **7742**, 77420V.

Caroli, E., *et al.* (2019). *IEEE Nucl. Sci. Symp. Conf. Rec.* **9059948**.

Chen, H., Awadalla, S. A., Iniewski, K., Lu, P. H., Harris, F., Mackenzie, J., Hasanen, T., Chen, W., Redden, R., Bindley, G., Kuvvetli, I., Budtz-Jørgensen, C., Luke, P., Amman, M., Lee, J. S., Bolotnikov, A. E., Camarda, G. S., Cui, Y., Hossain, A. & James, R. B. (2008). *J. Appl. Phys.* **103**, 014903.

Del Sordo, S., Abbene, L., Caroli, E., Mancini, A. M., Zappettini, A. & Ubertini, P. (2009). *Sensors* **9**, 3491–3526.

Del Sordo, S., Strazzeri, M., Agnetta, G., Biondo, B., Celi, F., Giarrusso, S., Mangano, A., Russo, F., Caroli, E., Donati, A., Schiavone, F., Stephen, J. B., Ventura, G., Abbene, L., Fauci, F., Raso, G. & Pareschi, G. (2004). *Nuov. Cim. B*, **119**, 257–270.

Devanathan, R., Corrales, L. R., Gao, F. & Weber, W. J. (2006). *Nucl. Instrum. Methods Phys. Res. A*, **565**, 637–649.

Drezet, A., Monnet, O., Mathy, F., Montemont, G. & Verger, L. (2007). *Nucl. Instrum. Methods Phys. Res. A*, **571**, 465–470.

Fatemi, S. *et al.* (2018). *IEEE Nucl. Sci. Symp. Conf. Rec.* **8824381**.

Gaskin, J. A., Sharma, D. P. & Ramsey, B. D. (2003). *Nucl. Instrum. Methods Phys. Res. A*, **505**, 122–125.

Gatti, E. & Rehak, P. (1984*a*). *Nucl. Instrum. Methods Phys. Res.* **225**, 608–614.

Gatti, E., Rehak, P. & Walton, J. T. (1984*b*). *Nucl. Instrum. Methods Phys. Res. A*, **226**, 129–141.

Gerardi, G. & Abbene, L. (2014). *Nucl. Instrum. Methods Phys. Res. A*, **768**, 46–54.

Guerra, P., Santos, A. & Darambara, D. G. (2008). *Phys. Med. Biol.* **53**, 1099–1113.

He, Z. (2001). *Nucl. Instrum. Methods Phys. Res. A*, **463**, 250–267.

He, Z., Li, W., Knoll, G. F., Wehe, D. K., Berry, J. & Stahle, C. M. (1999). *Nucl. Instrum. Methods Phys. Res. A*, **422**, 173–178.

Howalt Owe, S., Kuvvetli, I., Budtz-Jørgensen, C. & Zoglauer, A. (2019). *J. Instrum.* **14**, C01020.

Iniewski, K. (2014). *J. Instrum.* **9**, C11001.

Johns, P. M. & Nino, J. C. (2019). *J. Appl. Phys.* **126**, 040902.

Kalemci, E. & Matteson, J. L. (2002). *Nucl. Instrum. Methods Phys. Res. A*, **478**, 527–537.

Kim, J. C., Anderson, S. E., Kaye, W., Zhang, F., Zhu, Y., Kaye, S. J. & He, Z. (2011). *Nucl. Instrum. Methods Phys. Res. A*, **654**, 233–243.

Kim, J. C., *et al.* (2014). *J. Korean Phys. Soc.* **64**, 1136–1345.

Knoll, G. F. (2000). *Radiation Detection and Measurement*. New York: John Wiley.

Kuvvetli, I. & Budtz-Jorgensen, C. (2005). *IEEE Trans. Nucl. Sci.* **52**, 1975–1981.

Kuvvetli, I., Budtz-Jørgensen, C., Caroli, E. & Auricchio, N. (2010). *Nucl. Instrum. Methods Phys. Res. A*, **624**, 486–491.

Lingren, C. L., Apotovsky, B., Butler, J. F., Conwell, R., Doty, F. P., Friesenhahn, S. J., Oganesyan, A., Pi, B. & Zhao, S. (1998). *IEEE Trans. Nucl. Sci.* **45**, 433–437.

Owens, A., den Hartog, R., Quarati, F., Gostilo, V., Kondratjev, V., Loupilov, A., Kozorezov, A. G., Wigmore, J. K., Webb, A. & Welter, E. (2007). *J. Appl. Phys.* **102**, 054505.

Owens, A. & Peacock, A. (2004). *Nucl. Instrum. Methods Phys. Res. A*, **531**, 18–37.

Peng, H. & Levin, C. S. (2010). *Phys. Med. Biol.* **55**, 2761–2788.

Principato, F., Turturici, A. A., Gallo, M. & Abbene, L. (2013). *Nucl. Instrum. Methods Phys. Res. A*, **730**, 141–145.

Prokesch, M., Soldner, S. A. & Sundaram, A. G. (2018). *J. Appl. Phys.* **124**, 044503.

Ramo, S. (1939). *Proc. IRE*, **27**, 584.

Shockley, W. (1938). *J. Appl. Phys.* **9**, 635–636.

Szeles, C., Soldner, S. A., Vydrin, S., Graves, J. & Bale, D. S. (2008). *IEEE Trans. Nucl. Sci.* **55**, 572–582.

Takahashi, T. & Watanabe, S. (2001). *IEEE Trans. Nucl. Sci.* **48**, 950–959.

Thomas, B., Veale, M. C., Wilson, M. D., Seller, P., Schneider, A. & Iniewski, K. (2017). *J. Instrum.* **12**, C12045.

Turturici, A. A., Abbene, L., Gerardi, G. & Principato, F. (2014). *Nucl. Instrum. Methods Phys. Res. A*, **763**, 476–482.

Van Pamelen, M. A. J. & Budtz-Jørgensen, C. (1998). *Nucl. Instrum. Methods Phys. Res. A*, **403**, 390–398.

Veale, M. C., Booker, P., Cross, S., Hart, M. D., Jowitt, L., Lipp, J., Schneider, A., Seller, P., Wheater, R. M., Wilson, M. D., Hansson, C. C. T., Iniewski, K., Marthandam, P. & Prekas, G. (2020). *Sensors*, **20**, 2747.

Verger, L., Gros d'Aillon, E., Monnet, O., Montémont, G. & Pelliciari, B. (2007). *Nucl. Instrum. Methods Phys. Res. A*, **571**, 33–43.

Wahl, C. G. & He, Z. (2011). *IEEE Trans. Nucl. Sci.* **58**, 605–613.

Wahl, C. G., Kaye, W. R., Wang, W., Zhang, F., Jaworski, J. M., King, A., Boucher, Y. A. & He, Z. (2015). *Nucl. Instrum. Methods Phys. Res. A*, **784**, 377–381.

Yin, Y., Chen, X., Wu, H., Komarov, S., Garson, A., Li, Q., Guo, Q., Krawczynski, H., Meng, L. J. & Tai, Y. C. (2013). *IEEE Trans. Nucl. Sci.* **60**, 9–15.

Zappettini, A., Zha, M., Marchini, L., Calestani, D., Mosca, R., Gombia, E., Zanotti, L., Zanichelli, M., Pavesi, M., Auricchio, N. & Caroli, E. (2009). *IEEE Trans. Nucl. Sci.* **56**, 1743–1746.

Zhang, F., Herman, C., He, Z., De Geronimo, G., Vernon, E. & Fried, J. (2012). *IEEE Trans. Nucl. Sci.* **59**, 236–242.

Zhu, Y., Anderson, S. E. & He, Z. (2011). *IEEE Trans. Nucl. Sci.* **58**, 1400–1409.